Electronic Supplementary Information

Experiment Section

Model catalyst synthesis

Briefly, Co_3O_4 nanoparticles were synthesized on a stable Ti plate (purity: 99.999%, thickness: 0.4 mm) via the facile decomposition of $Co(NO_3)_2$ solution (2.5 M) at 250 °C in the air (muffle furnace: Hefei Kejing Material Technology Co., Ltd., KSL-1200X) for 12 h. The resultant Co_3O_4/Ti was sonicated (ultrasonic cleaner: KUNSHAN ULTRASONIC INSTRUMENT Co., Ltd., KQ2200DE) in ultrapure water (ultrapure water machine: Sichuan ULUPURE Ultrapure Technology Co., Ltd., UPT-1-10T, resistivity: 18.25 MΩ.cm, ~25°C) for 10 s to remove loosely connected particles, and the turbid liquid was poured off. Repeat this step 2 or 3 times with ultrapure water until no visible particles fall off. Finally, at room temperature, the Co_3O_4/Ti was washed with ethanol and dried naturally.

Ex situ/In situ catalyst characterization

The crystal phase structures were recorded on a DX-2700BH X-ray diffractometer (DANDONG HAOYUAN INSTRUMENT Co., Ltd., Cu Kα radiation, 2θ range = 10–80°, step width = 0.02°) with a Dwlc-3 Water circulating system. The catalyst morphology was acquired by using a Gemini SEM 300 electron microscope (ZEISS, Germany). The catalyst surface chemistry was investigated using XPS (Thermo Scientific™ Nexsa™, USA) with a monochromatic X-ray source (Al Kα hυ = 1486.6 eV). All XPS data were corrected by C 1s line at 284.8 eV. The catalyst mass loading and Co dissolution after electrolysis were determined by inductively coupled plasma optical emission spectrometer (ICP-OES, PerkinElmer Avio 200). In situ Raman spectra were recorded with a LabRAM HR Raman spectrometer (Horiba) equipped with a ×50 objective and a 633 nm He-Ne laser. The tests were carried out using a custom cell with a three-electrode system consisting of Ti plate supported Co_3O_4 as the working electrode, Ag/AgCl (Saturated KCl) as the reference electrode, and graphite rod as the counter electrode. Operando EPR was recorded on a Bruker

EMX plus X-band EPR spectrometer. For spin trapping radicals by 5,5-dimethyl-1-pyrroline-N-oxide (DMPO), chronoamperometric tests were performed at a fixed potential of 2.1 V for 1 min, and 100 mM DMPO was added into the electrolyte during the reaction. Co_3O_4/Ti was directly used as the working electrode, a graphite rod was used as the counter electrode, and a SCE was used as the reference electrode. After that, the solution was taken out for the EPR test.

Electrochemical tests

NOOR and eCOR-NOOR performance tests were performed in a three-electrode system (~25°C) on CHI 660E electrochemical workstation. A piece of monolithic Co_3O_4/Ti (0.5 × 0.5 cm^2) was directly used as the working electrode, and a SCE and a graphite rod electrode (φ: 5 mm) were employed as the reference electrode and counter electrode, respectively. All current densities were calculated based on the geometrical surface area of the electrodes. Unless otherwise specified, the scan rate for all polarization tests was set as 2 mV s^{-1}. Prior to any measurement, the electrolyte was saturated by bubbling Ar (99.9999%, flow rate was maintained at 50 sccm using a Sevenstar® mass flow controller) for at least 20 min to remove the oxygen dissolved in the electrolyte and in the headspace of the electrolyzer chambers. The electrolyte was 0.01 M $HClO_4$ with different concentrations of NaCl if no special instruction. EIS was performed over a wide frequency range from, and AC amplitude was set as 5 mV. In this work, potentials are mostly reported versus SCE and are not adjusted by iR compensation if no special instruction is given. The potentials can be calibrated to the reversible hydrogen electrode (RHE) reference scale using the formulas: E (vs. RHE) = E (vs. SCE) + 0.059 × pH + 0.2412 V. For RRDE measurements, a glassy carbon electrode, a SCE and a graphite rod electrode (φ: 5 mm) were employed as the working electrode, reference electrode, and counter electrode, respectively. The inks (10 mg mL^{-1}) were prepared by sonicating powder catalyst, Nafion solution (Sigma Aldrich), ultrapure water, and ethanol. For the two-electrode electrolysis measurements, we used a commercial platinum plate electrode (1 × 1 cm^2) as the cathode to ensure better reproducibility. The real exhaust gas is obtained from

commercial diesel engines (Jiangsu Bainianchang Diesel Engine Import and Export Co., Ltd.). The real exhaust gas enters the anodic chamber by first filtering out some of the larger particles through a sealed unit containing ultrapure water.

Product analysis

An online gas chromatograph (SHIMADZU GC-2014C) was used to analyze the amount of evolved H_2 during the reaction (Ar was used as the carrier gas). The eCOR-NOOR data were recorded while simultaneously collecting the H_2. An air-tight electrochemical cell with two gas inlets and two gas outlets was used for the GC measurement, and a mixed gas of NO/Ar (10 vol% NO) and 99.9999% Ar were used as the inlet gas for the anodic and cathodic chamber, respectively. The cathode and anode were also separated with a proton membrane to prevent the interchange of gases. The standard gasses (Dalian Special Gases Co., Ltd.) of a series of H_2 concentrations (20. 07 ppm, 101.1 ppm, 200.44 ppm, 1005.01 ppm, 10061.82 ppm, 19906.09 ppm) were injected into the GC-2014C for calculating the standard curve. The concentration of active chlorine after eCOR was examined by a DPD assay. UV-Vis spectrophotometer (SHIMADZU UV-2700) was used to analyze the aqueous product content of the eCOR, NOOR, and eCOR-NOOR.

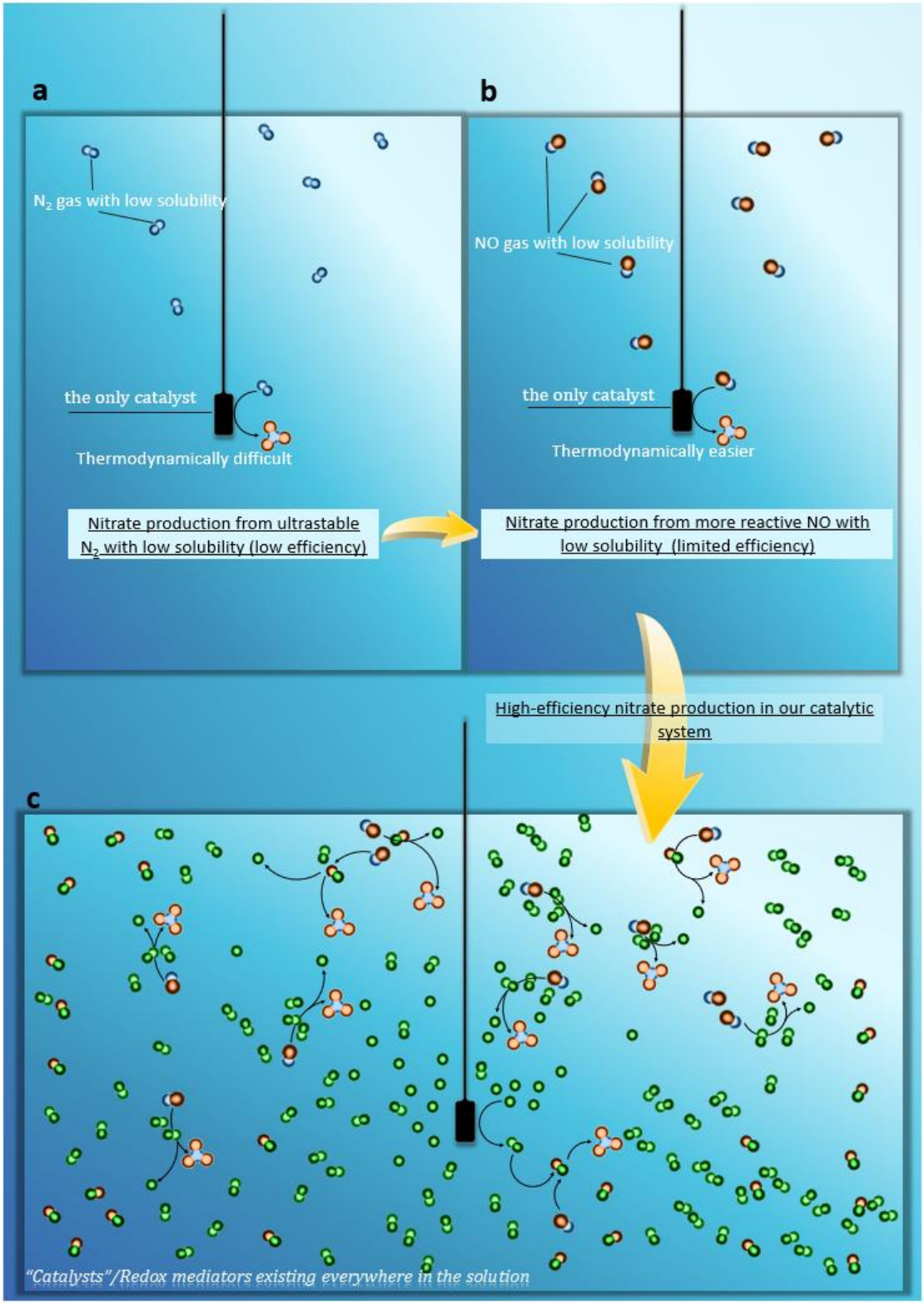

Fig. S1. The comparison of the recently reported (a) eN_2OR, (b) eNOOR and (c) our eCOR-NOOR systems. See below for a detailed explanation.

N_2 has attracted attention as a potential feedstock for the electrosynthesis of nitric acid and nitrate (such as: *Science* 2018, **360**, eaar6611, *Angew. Chem., Int. Ed.* 2022,

61, e202115409, *Adv. Mater.* 2020, **32**, 2002189, *ACS Catal.* 2021, **11**, 14032–14037, *ACS Nano* 2022, **16**, 655–663, *Adv. Mater.* 2022, **34**, 2108180) because of its great abundance (~ 78% of the atmosphere's volume), but unfortunately, N_2 is one of the most stable molecules with ultralow solubility (*Chem. Rev.* 1977, **77**, 219–262, *J. Phys. Ref. Data* 1984, **13**, 563–600, see Fig. S1a). It is both energetically and kinetically disadvantageous for complete N_2-to-NO_3^- conversion.

Thermodynamically, NO is much more reactive than N_2, and it has an unpaired electron $\{(\sigma 2s)^2(\sigma^* 2s)^2(\sigma 2px)^2(\pi 2py)^2(\pi 2pz)^2(\pi^* 2py)^1\}$ that makes it both an electron donor and an acceptor. In addition, NO pollution affects the environment, leading to acid rain, photochemical smog, and a series of NO-triggered human health issues. Hence, the abatement of NO into useful nitrate via electrocatalysis is a viable strategy from the standpoint of less energy consumption and "turn waste into treasure".

While the electrocatalytic NO conversion (Fig. S1b) may offer a highly attractive route for NO_3^- synthesis, along with the potential to alleviate NO-triggered pollution, two big challenges remain. Firstly, electrochemical oxidation or reduction of NO on heterogeneous catalysts, *i.e.*, an electrode, must suffer from the poor solubility of NO in aqueous electrolytes (*Atmos. Chem. Phys.* 2015, **15**, 4399–4981). Since fairly few NO gas reactants can be supplied to active sites of catalysts, establishing efficient eNOOR or eNORR is extremely hard. Our group and others reported that the use of metal complexes to increase NO solubility for electrochemical NO conversion (such as: *Chem. Commun.* 2021, **57**, 13562–13565, *Angew. Chem. Int. Ed.* 2021, **60**, 25263–25268, *ACS Energy Lett.* 2020, **5**, 3647–3656, and *J. Hazard. Mater.* 2022, **430,** 128451), but the conversion rates are still not satisfactory. Secondly, the concentration of NO is usually very low (<5%) (e.g., flue gases and vehicle exhausts) is low, which will further reduce the conversion efficiency. In fact, many previous studies on electrochemical conversion of NO have used highly concentrated NO (>99%) as the feeding gas (such as: *Angew. Chem. Int. Ed.* 2021, **60**, 24605–24611, *Angew. Chem. Int. Ed.* 2020, **59**, 9711–9718, *Adv. Sci.* 2022, **9**, 2201410., and *Nano Res.* 2022, **15**, 8890–8896), which is not conducive to practical applications. If high-purity NO is one of the preconditions for the conversion to efficiently occur,

more extra facilities for concentrating NO gas must be required; nonetheless, the industrial-scale applications require simple reaction systems.

Genuinely efficient but simple eCOR-NOOR systems (Fig. 1c) present a series of advantages toward sustainable NO_3^- synthesis:

(i) From one catalyst to countless catalysts (i.e., redox mediators): In the eCOR-NOOR process, the chlorine-containing species act as highly soluble redox mediators/shuttles between the electrode and NO. They donate electrons to the electrode, giving an oxidized state of chlorine. Following such oxidation, the catalysts (i.e., active chlorine) accept electrons from NO in the electrolyte solution and finally return to the initial state (i.e., Cl^-). Notably, this expands the active site from limited 2D electrode surfaces to almost all corners of the entire 3D electrolyte.

(ii) Abundant chlorine on Earth: The cheap and easy availability of Cl^- makes eCOR-NOOR (including heterogeneous eNOOR) technology more practical than heterogeneous eNOOR (*Angew. Chem. Int. Ed.* 2021, **60**, 24605–24611). The electro-oxidation of NO (even NO_2, N_2O_3, NO_2^-) at the electrode occurs simultaneously with the oxidation reactions in electrolyte solution and can achieve maximum conversion efficiency.

(iii) Unlike the harsh condition of the HBP and Ostwald process, the whole process of eCOR-NOOR is carried out under ambient conditions. The simple but highly effective electrolytic device is different from the complex HBP and Ostwald process. Moreover, the eCOR-NOOR does not generate additional greenhouse gas emissions (such as N_2O). The exhaust gas can be used as a raw material for eCOR-NOOR catalysis in a simple electrolytic cell. The high-purity H_2 produced at the anode can be directly used as a green fuel.

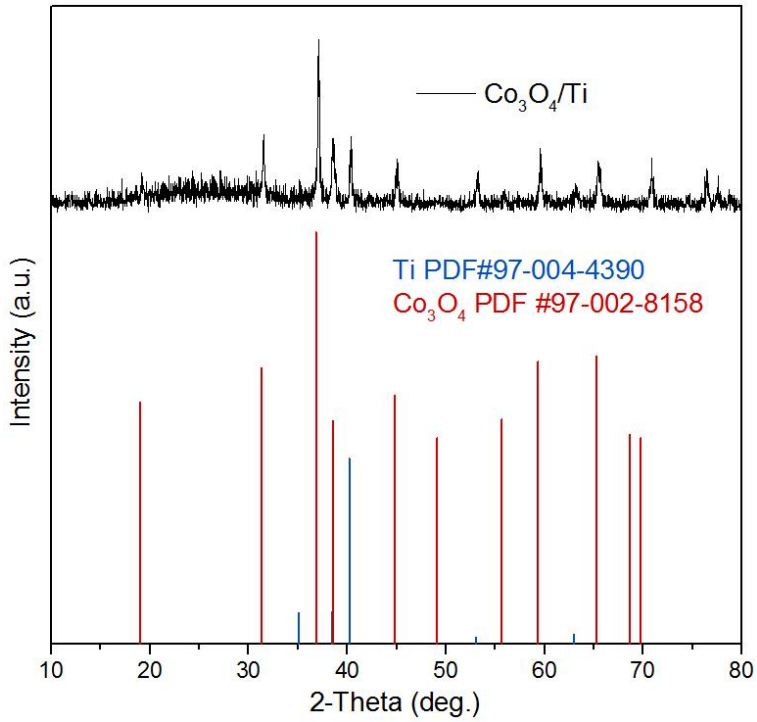

Fig. S2. XRD diffraction pattern of Co_3O_4/Ti. The pattern shows characteristic peaks for the Ti substrate and Co_3O_4 nanoparticles.

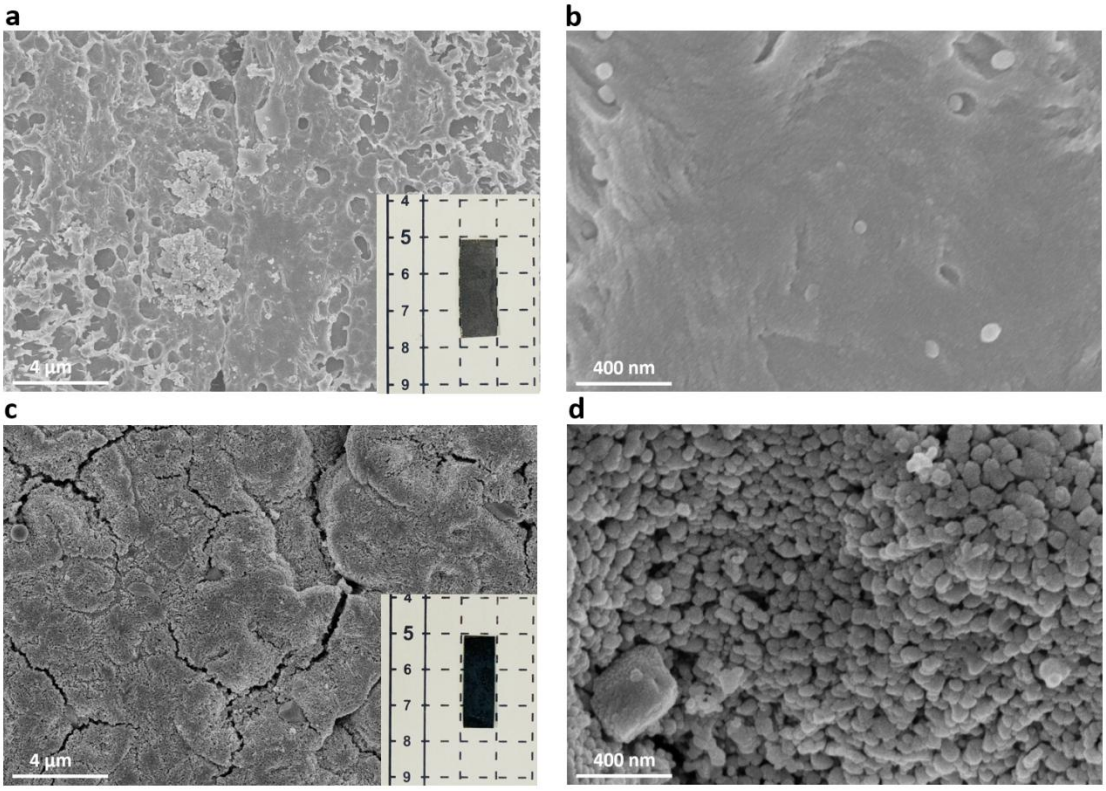

Fig. S3. Characterizations of the model electrocatalyst Co_3O_4/Ti and bare Ti plate. (a) Low- and (b) high-magnification SEM images of bare Ti plate (thickness: 2 mm). The inset image in (a) shows the photograph of the fresh Ti plate after acid treatment. (c) Low- and (d) high-magnification SEM images of Co_3O_4/Ti. The inset image in (c) shows the photograph of the Co_3O_4/Ti.

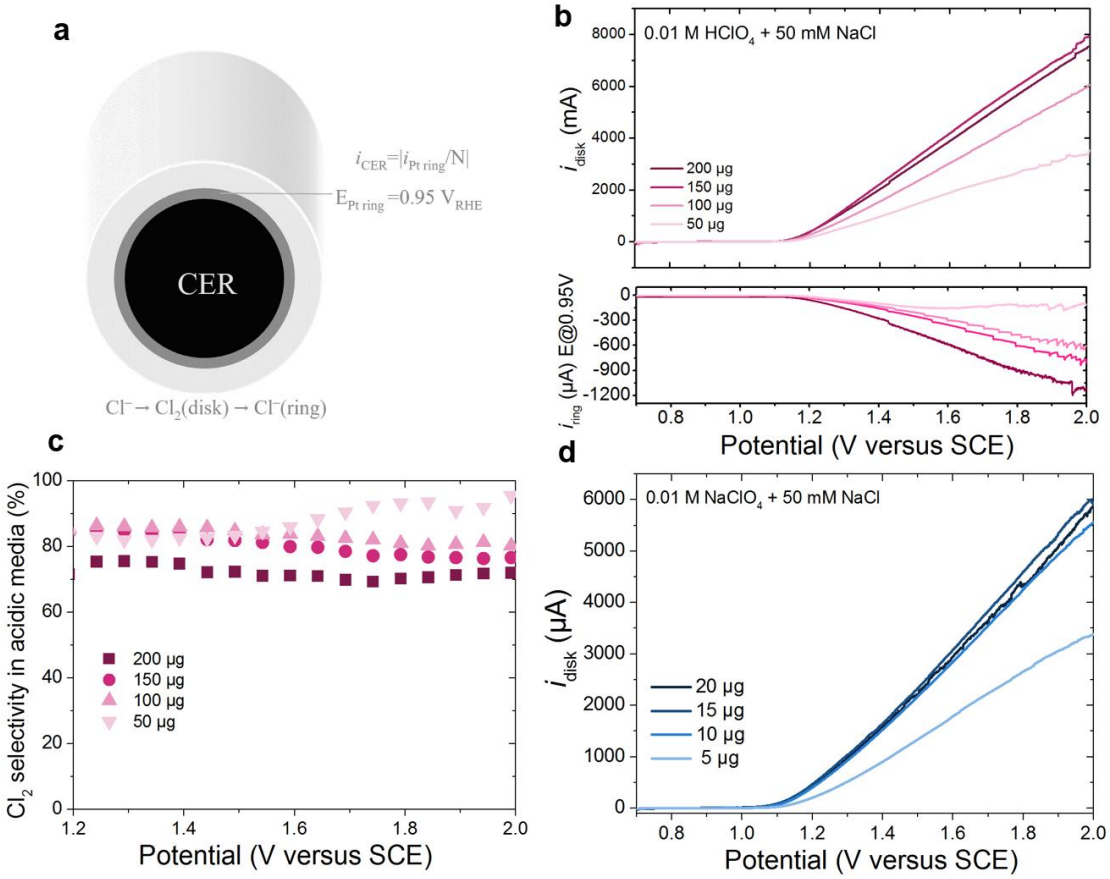

Fig. S4. (a) Schematic of RRDE measurement of eCOR in acidic media. The effect of mass loading on (b) current density (i_{disk} and i_{ring}) and (c) selectivity in acidic solution. (d) The effect of mass loading on current density in neutral solution.

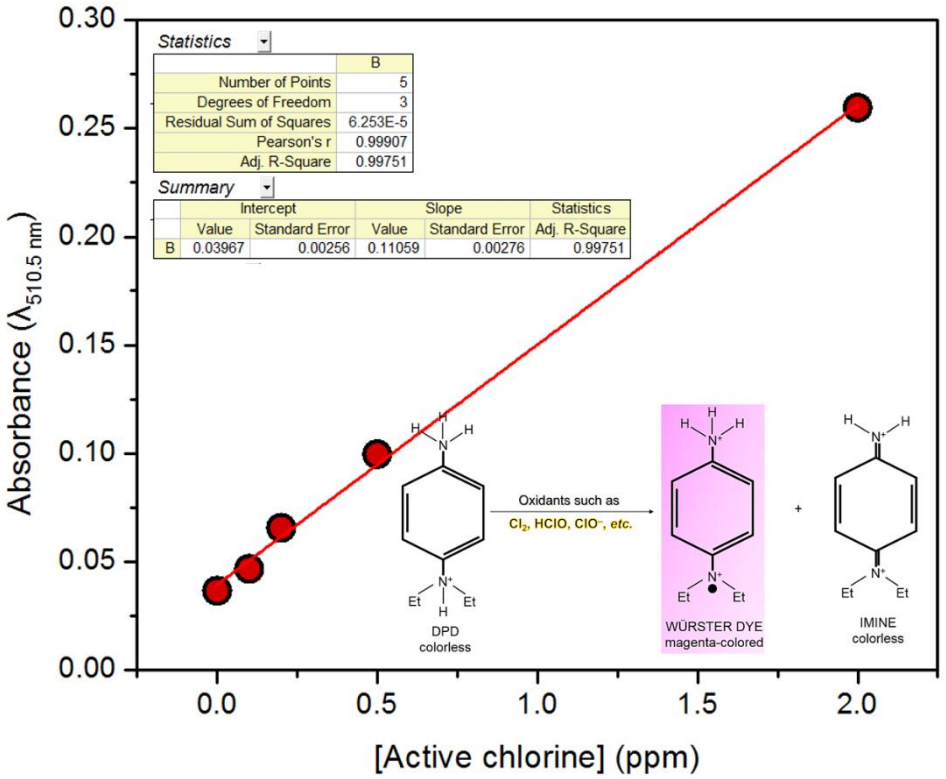

Fig. S5. Standard curve fitting for DPD assay (maximum absorption at $\lambda_{max,abs}$= 510.5 nm) at the following active chlorine concentrations: 0 ppm, 0.1 ppm, 0.2 ppm, 0.5 ppm, and 2 ppm. The working principle of DPD measurement is given as the inset.

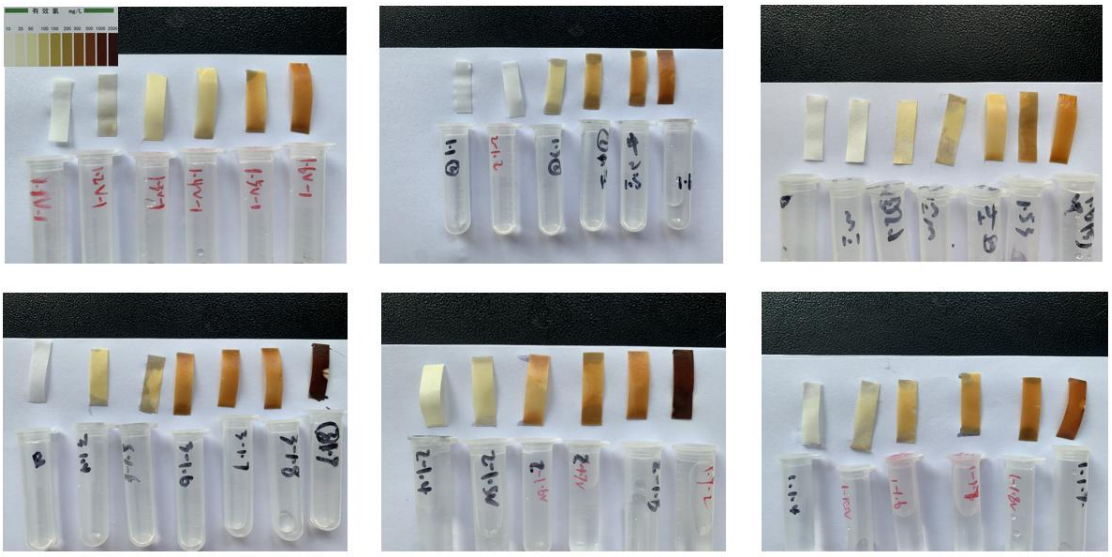

Fig. S6. Optical photographs of the active chlorine test strip (Shanghai Xinshengshi Chemical Technology Co., LTD) with the electrolyte added dropwise. The second-row photographs correspond to eCOR performed in the acidic electrolyte. The results of the test strip indicate that more active chlorine is produced in the acidic electrolyte than in the neutral electrolyte, which is in line with the results obtained by DPD method.

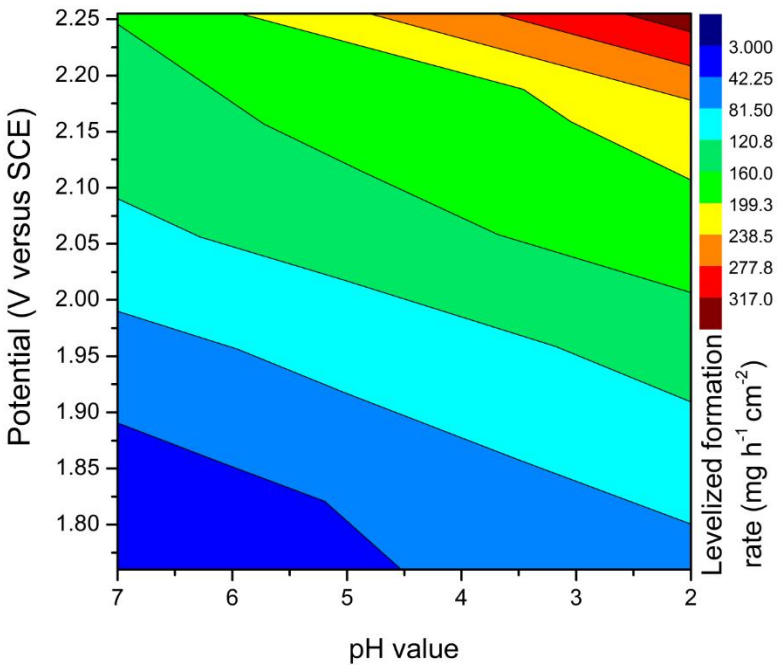

Fig. S7. Activity chlorine plots of eCOR at the fixed Cl^- concentration, using applied potential and pH value as the descriptors. Lower pH and higher potentials benefit the eCOR.

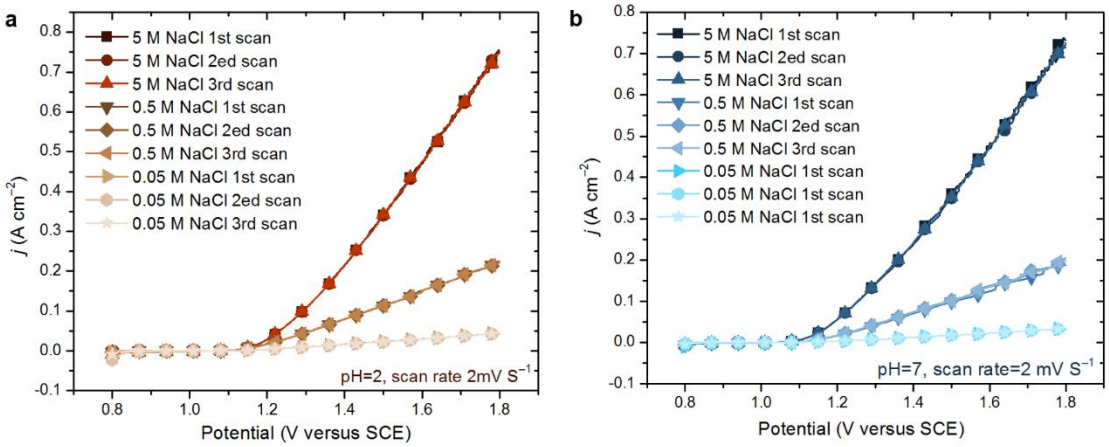

Fig. S8. LSV plots of eCOR at the scan rate of 2mV s^{-1} recorded in (a) acidic and (b) neutral media.

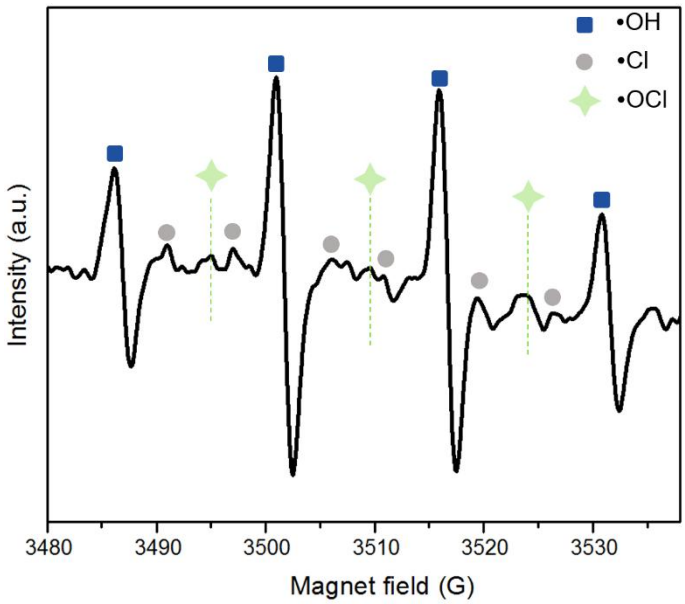

Fig. S9. Operando EPR plot during eCOR, with the addition of DMPO as radical capture reagent (*Water Res.* 2020, **170**, 115357 and *Electrochim. Acta* 2019, **297**, 1–9).

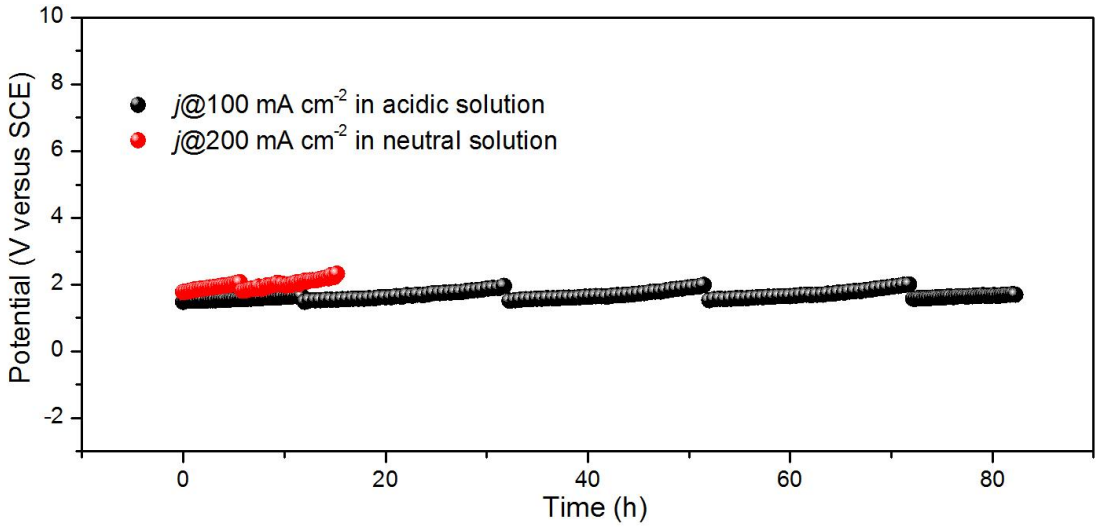

Fig. 10. Long-term stability tests of Co_3O_4/Ti for eCOR recorded in acidic (pH=2, black) and neutral (pH=7, red) solutions at room temperature.

We carried out chronopotentiometric measurements with a three-electrode system in acidic electrolyte. Although the potential shows relatively little increase after durability measurement at the *j* of 100 mA cm^{-2} (black lines), the potential would decrease again after changing the electrolyte, indicating that our model electrocatalyst was relatively stable. In addition, the current density was fixed at a higher *j* of 200 mA cm^{-2} to observe the potential decrease in the neutral solution (red curves in Fig. S10). The electrolysis time was shorter in the neutral electrolyte in that the demonstration was performed only to observe the trend of voltage increase and decrease. The voltage changes abruptly during the tests because the electrolyte was refreshed. Overall, the Co_3O_4/Ti exhibited excellent electrochemical stability for eCOR.

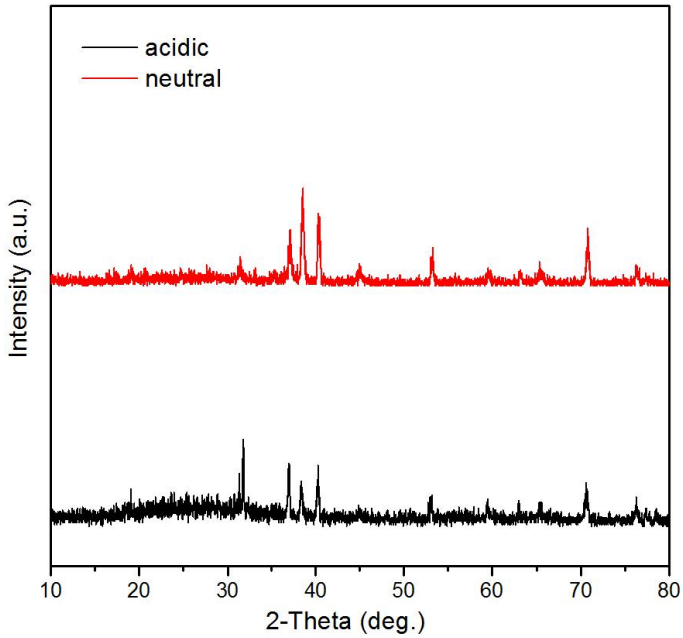

Fig. 11. XRD diffraction patterns of Co_3O_4/Ti after the eCOR stability tests in acidic and neutral solutions.

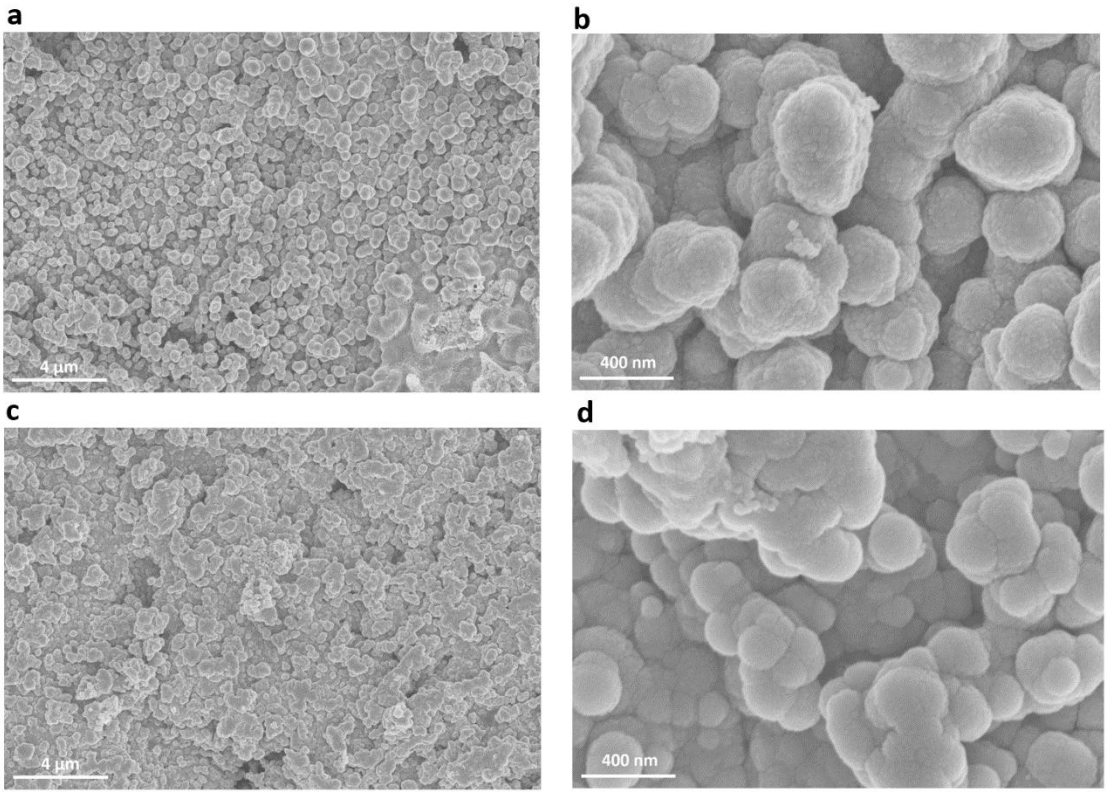

Fig. S12. (a) Low- and (b) high-magnification SEM images of Co_3O_4/Ti after eCOR electrolysis in acidic solution. (c) Low- and (d) high-magnification SEM images of Co_3O_4/Ti after eCOR electrolysis in neutral solution.

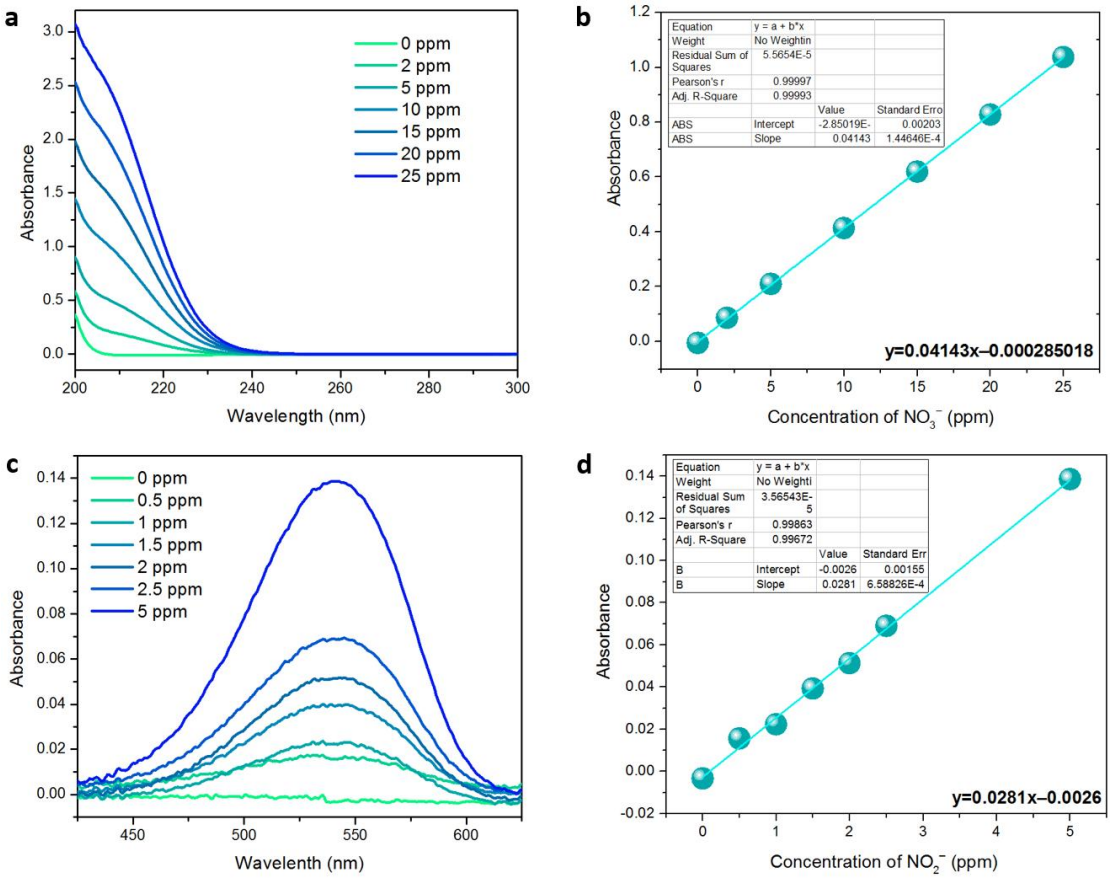

Fig. S13. (a) UV-Vis absorption spectra of standard solution with given NO_3^- concentrations. (b) Calibration curve used for calculation of NO_3^- concentrations. (c) UV-Vis absorption spectra of standard solution with given NO_2^- concentrations. (d) Calibration curve used for calculation of NO_2^- concentrations.

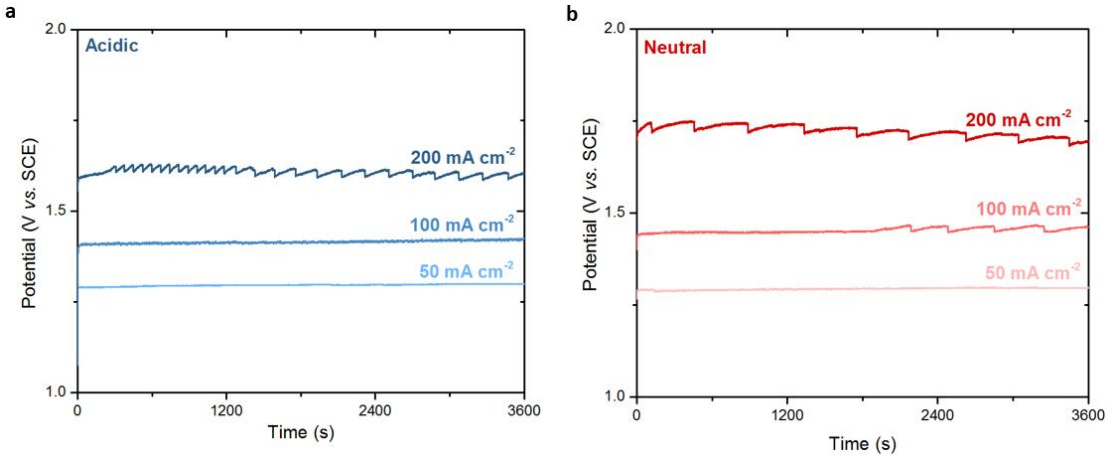

Fig. S14. Chronopotentiometric curves at a series of fixed j (*i.e.*, 200 mA cm^{-2}_{geo}, 100 mA $cm^{-2}_{geo,}$ 50 mA cm^{-2}_{geo}) in (a) acidic and (b) neutral electrolytes. The relatively stable curves illustrate the stability of the nanostructured Co_3O_4, and the jagged curves are caused by bubbles created by the high current.

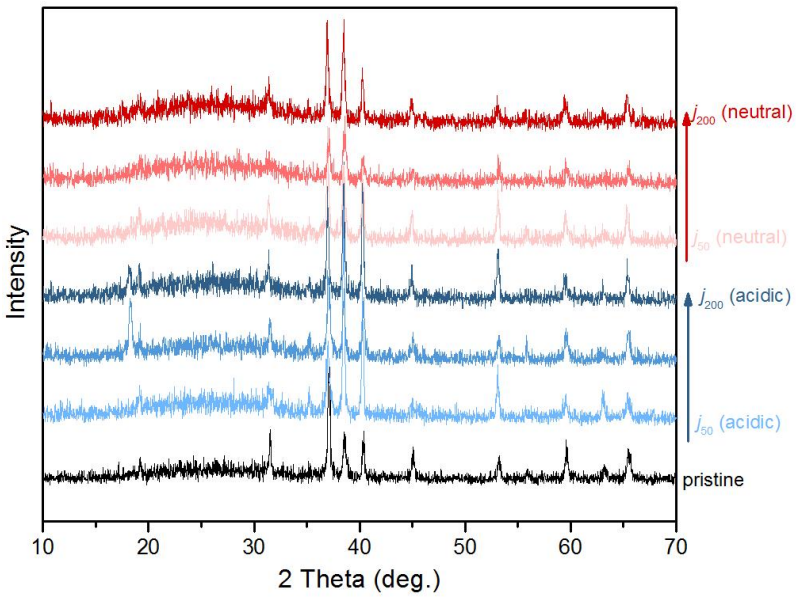

Fig. S15. XRD patterns of pristine Co_3O_4/Ti and post-electrolysis Co_3O_4/Ti for 50 mA cm^{-2}_{geo} (j_{50}) in acidic solution, j_{100} in acidic solution, j_{200} in acidic solution, j_{50} in neutral solution, j_{100} in neutral solution and j_{200} in neutral solution. The XRD patterns did not show any significant change nor shift in the observed peaks in both acidic and neutral media, still typical of Co_3O_{4c} and Ti. This suggests no major structural changes are occurring to the bulk of the Co_3O_4/Ti electrode.

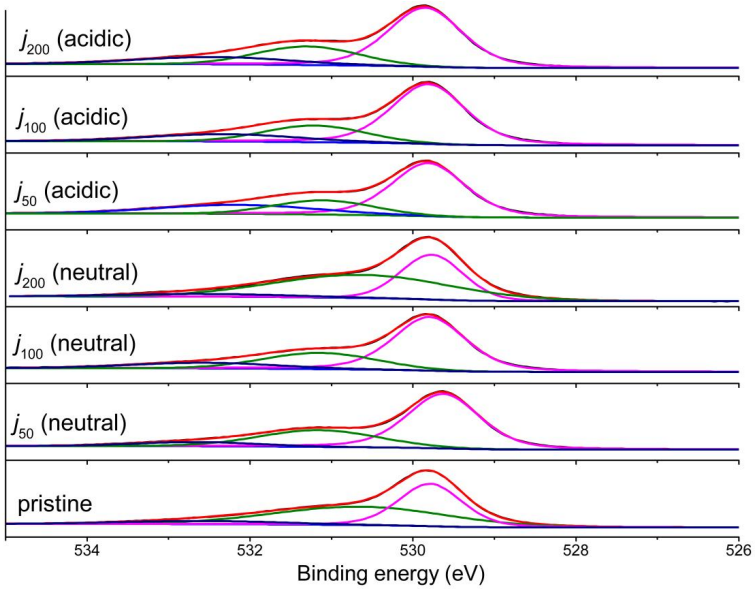

Fig. S16. Fits of high-resolution XPS spectra of the O 1s core level of the pristine Co_3O_4/Ti and post-eCOR-NOOR Co_3O_4/Ti after different electrolysis conditions. The O 1s signal contains one dominant peak, which can be fitted into lattice O, absorbed H_2O, and hydroxyl group at the binding energy of 529.6 eV, 531 eV, and 532.6 eV, respectively. The most significant change in the surface chemical state after the eCOR-NOOR processes is the formation of hydroxyl compounds on the surface, followed by absorbed H_2O and lattice O (*Nat. Commun.* 2015, **6**, 8625). Overall, the catalyst remains fairly stable.

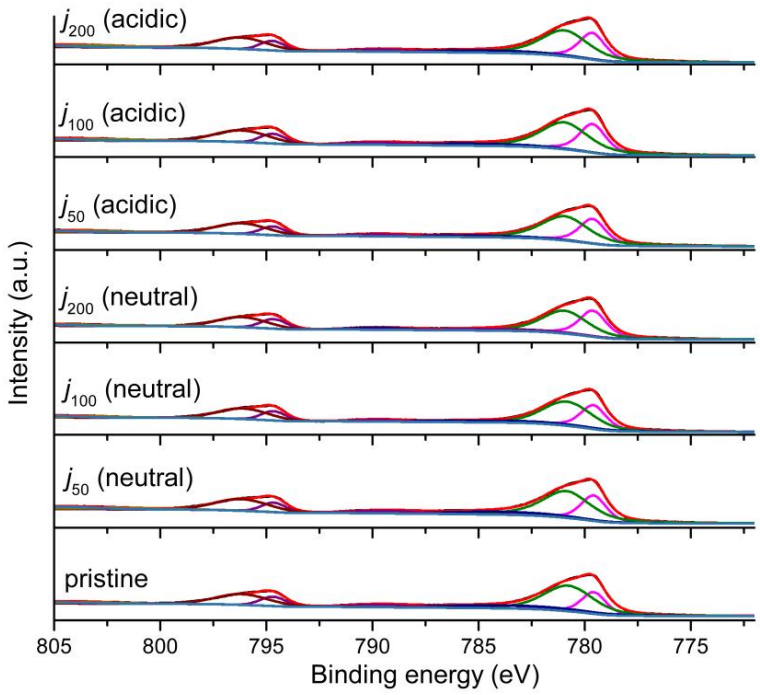

Fig. S17. High-resolution Co 2p XPS spectra of pristine Co_3O_4/Ti and Co_3O_4/Ti under different eCOR-NOOR testing conditions. The elemental compositions were mostly preserved after eCOR-NOOR testing (Table S5).

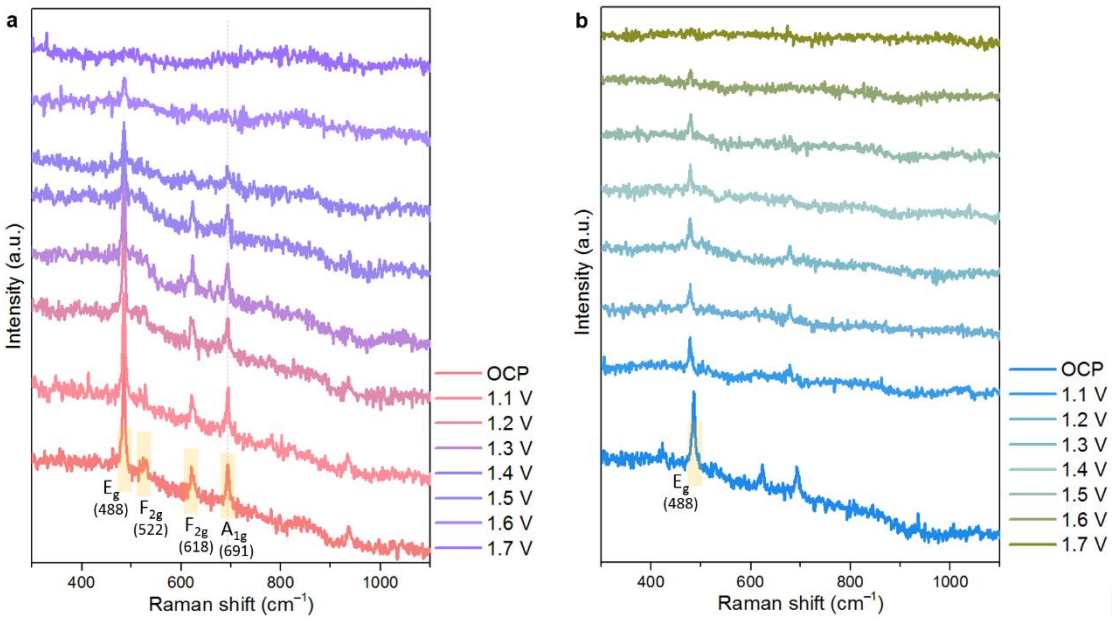

Fig. S18. In situ Raman characterizations of Co_3O_4/Ti during (a) eCOR and (b) eCOR-NOOR tests at various constant potentials (versus Ag/AgCl) without iR correction (increased from 1.0 to 1.7 V). Saturated NaCl solution (pH = 2) was used to provide enough Cl^- for eCOR catalysis and increase the intermediate number on the catalytic surface.

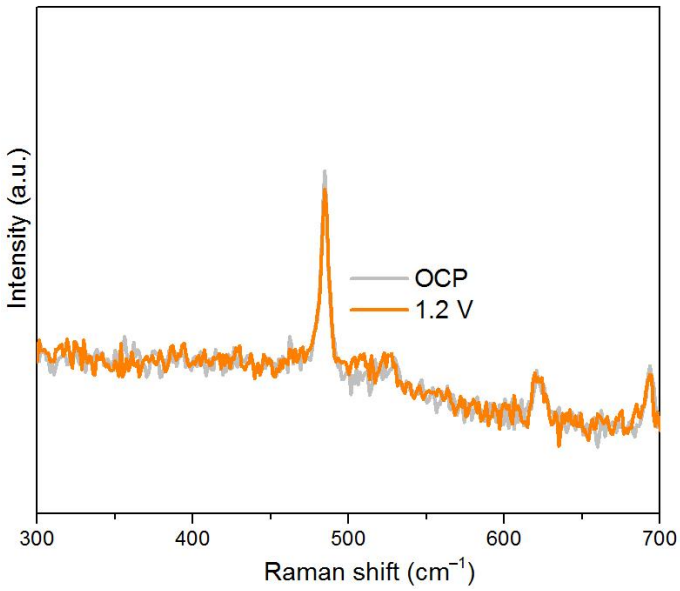

Fig. S19. In situ Raman spectra of Co_3O_4/Ti during eCOR at OPC and 1.2 V (versus Ag/AgCl).

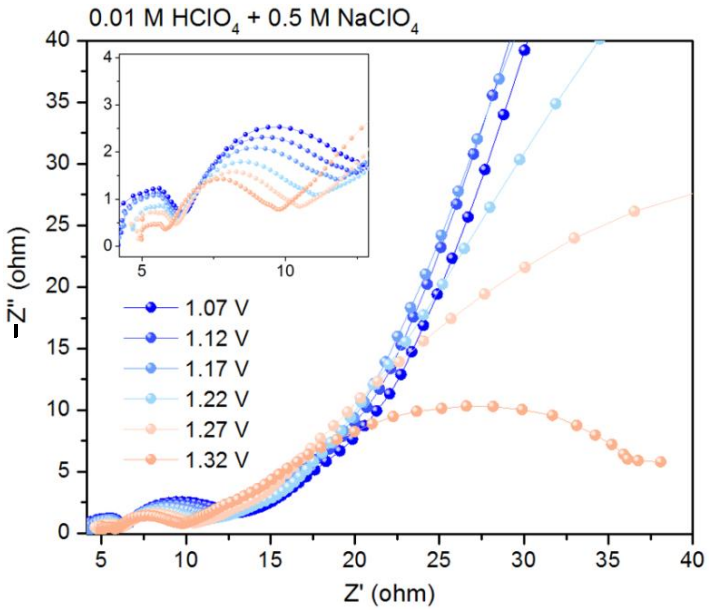

Fig. S20. In situ Nyquist plots of Co_3O_4/Ti at different potentials in 0.01 M $HClO_4$ + 0.5 M $NaClO_4$.

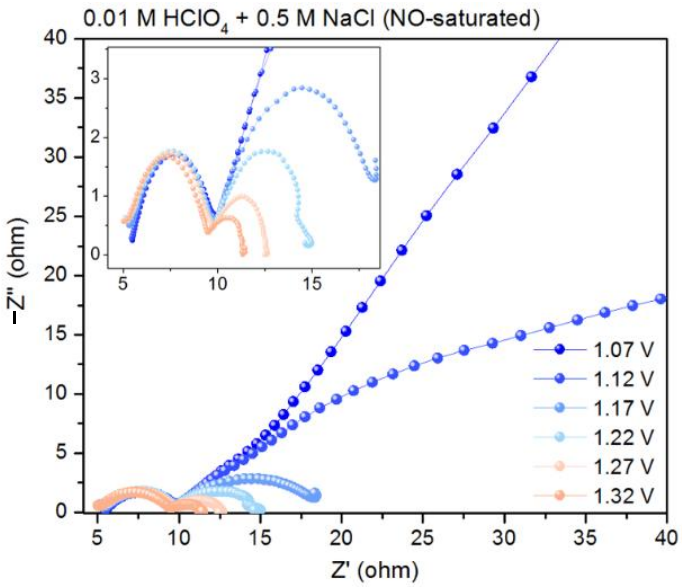

Fig. S21. In situ Nyquist plots of Co_3O_4/Ti at different potentials in NO-saturated electrolyte.

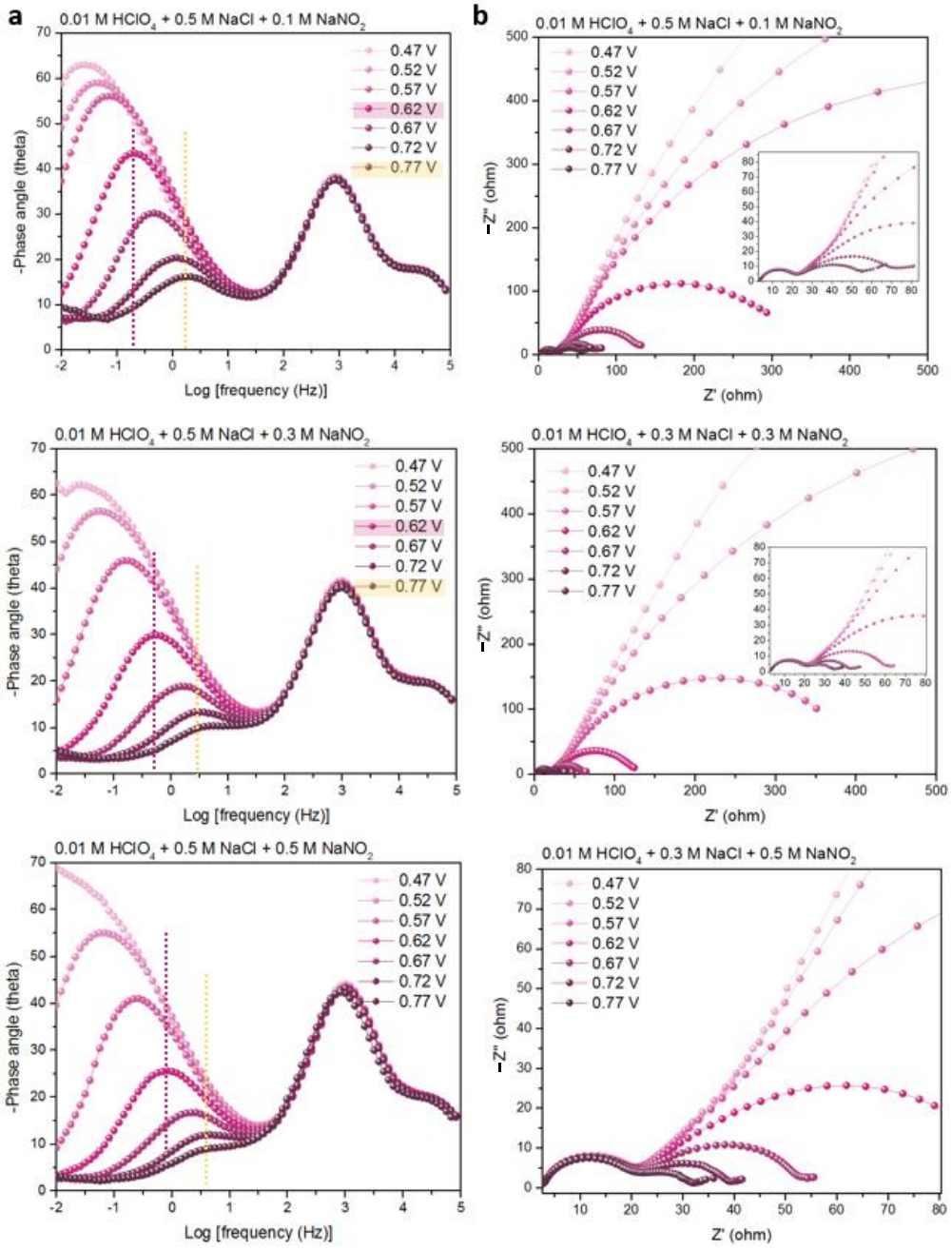

Fig. S22. (a) Impedance spectra and Bode phase plots (b) of Co_3O_4/Ti in 0.01 M $HClO_4$ solution with different concentrations of $NaNO_3$ (i.e., 0.1 M, 0.3 M, and 0.5 M).

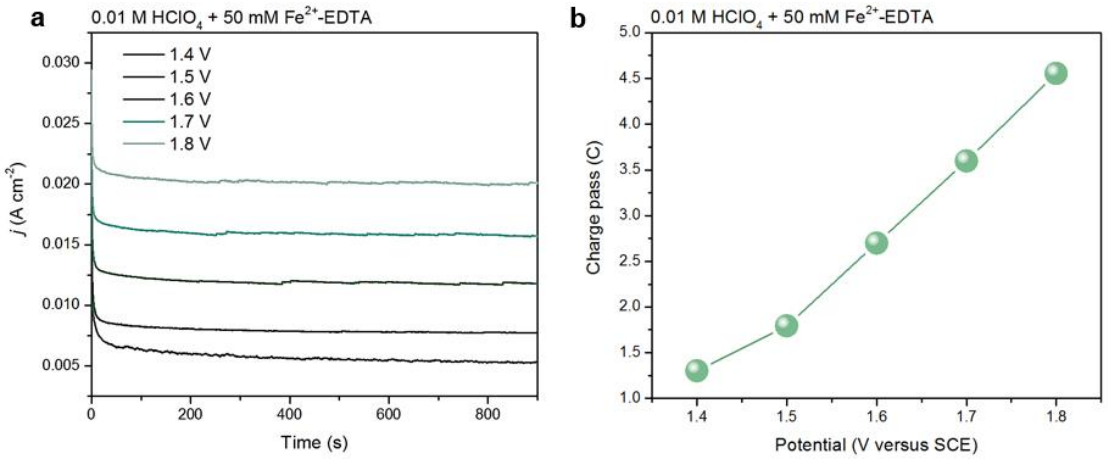

Fig. S23. (a) Chronoamperometric *j-t* curves after adding 50 mM Fe^{2+}–EDTA in the chloride-free electrolyte and (b) the charge accumulation at each potential. The low charge pass values (lower than 5 coulombs) indicate a limited conversion efficiency.

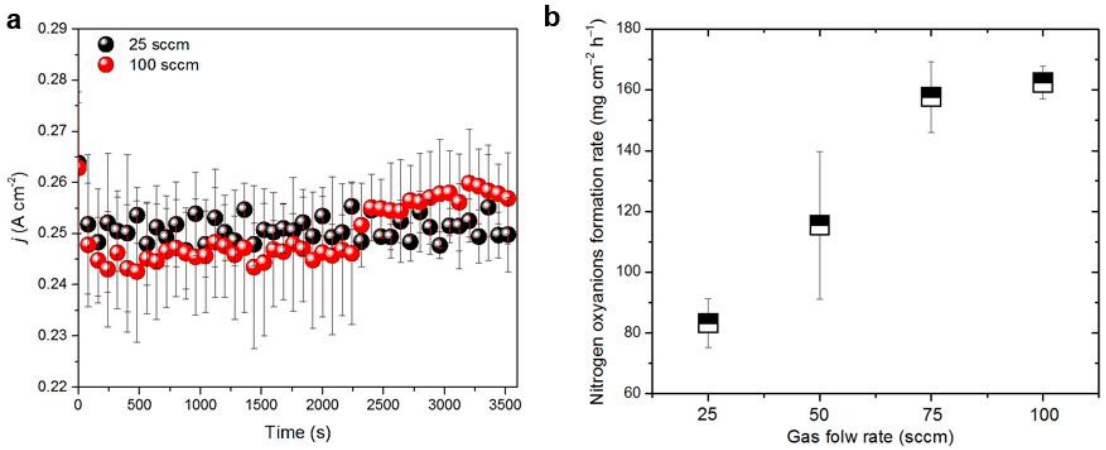

Fig. S24. (a) Effect of different flow rates (25 sccm versus 100 sccm) on the current densities. Since the reaction current mainly comes from the oxidation of chloride ions on the electrode surface. The flow rate of the inlet gat has less effect on it. (b) Higher flow rates lead to higher yields. This shows that our eCOR-NOOR system can adapt to a variety of exhaust flow rate scenarios.

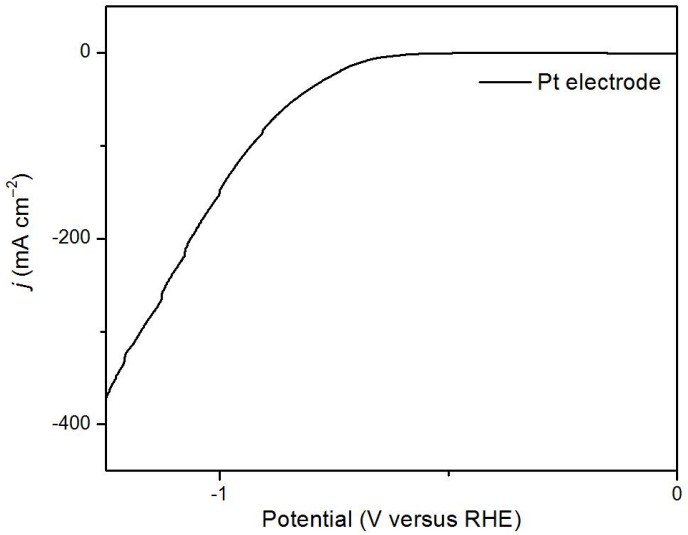

Fig. S25. Polarization curve of the commercial Pt electrode recorded in the neutral solution.

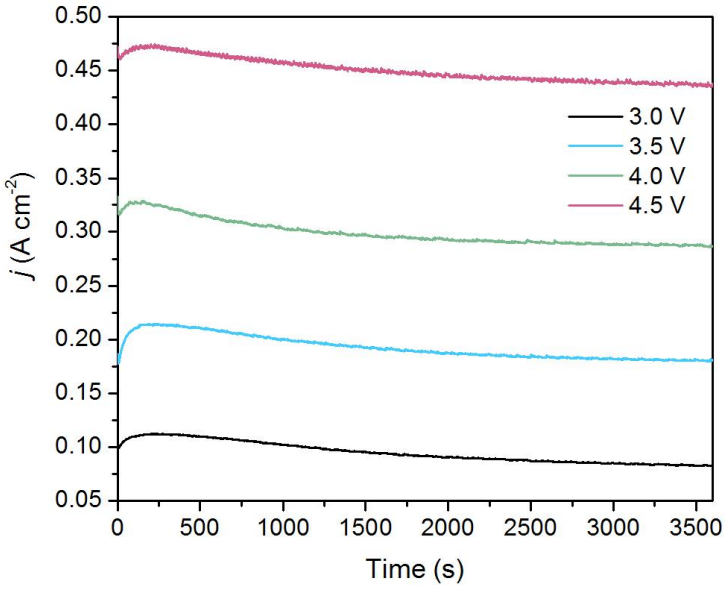

Fig. S26. Chronoamperometry curves for the full-cell electrolysis system at various potentials.

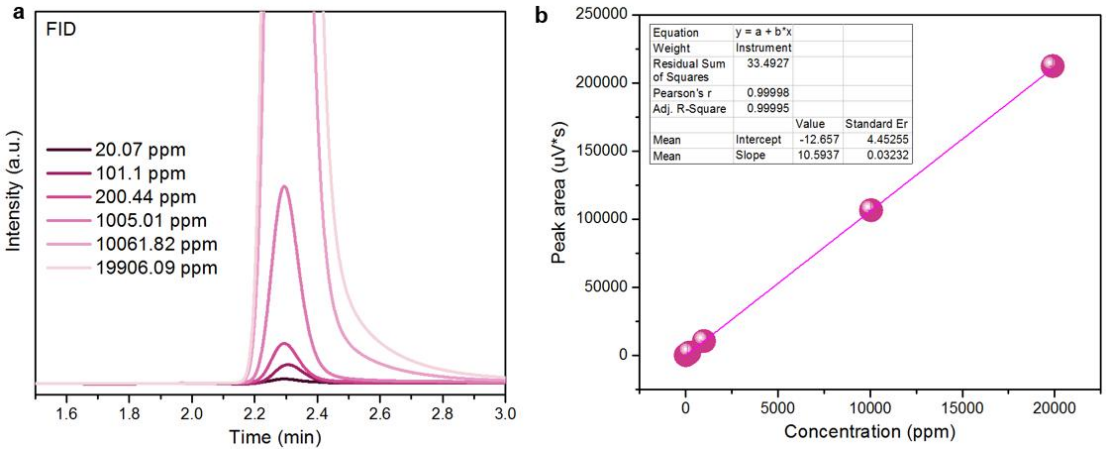

Fig. S27. (a) Gas chromatography curves and (b) the corresponding calibration curve of H_2 gas quantified using SHIMADZU GC-2014C.

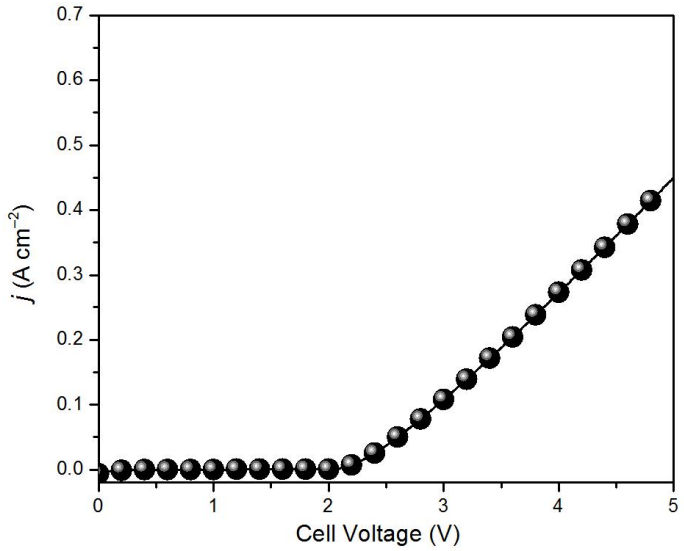

Fig. S28. Polarization curve of the two-electrode system after the long-term chronopotentiometric measurements (scan rate: 5 mV s^{-1}).

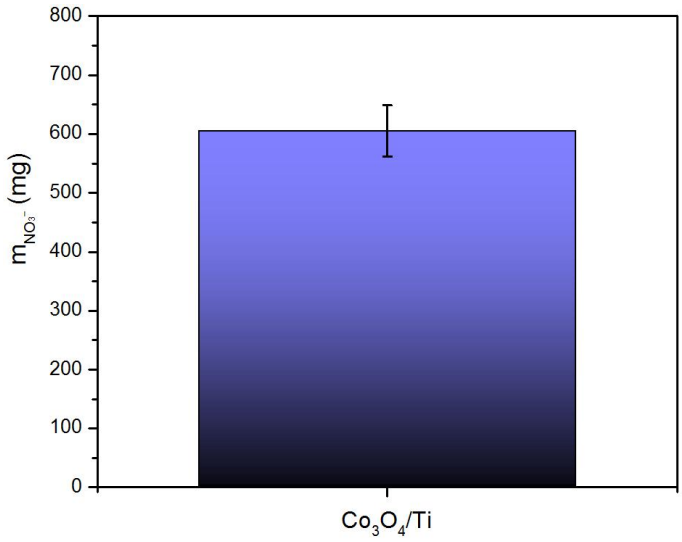

Fig. S29. Accumulation of NO_3^- in the anodic compartment after electrolysis at the fixed *j* of 100 mA cm for 10 h (NO concentration: 1%).

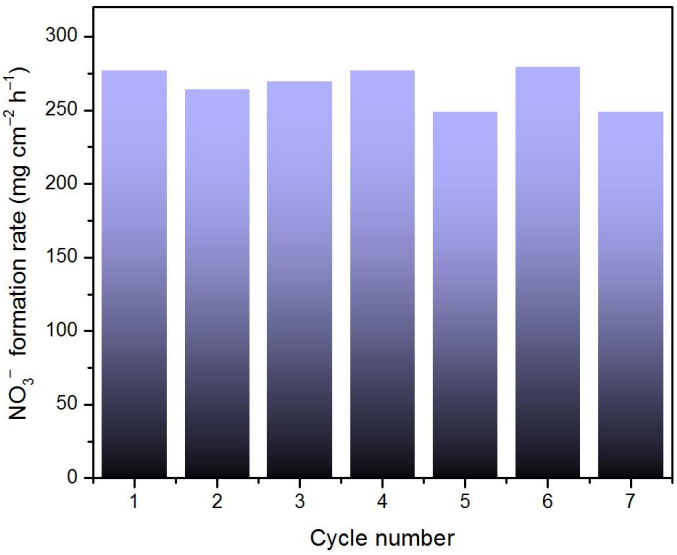

Fig. S30. Cycling stability test of the Co_3O_4/Ti electrode towards electrosynthesis of NO_3^- at the cell voltage of 3 V.

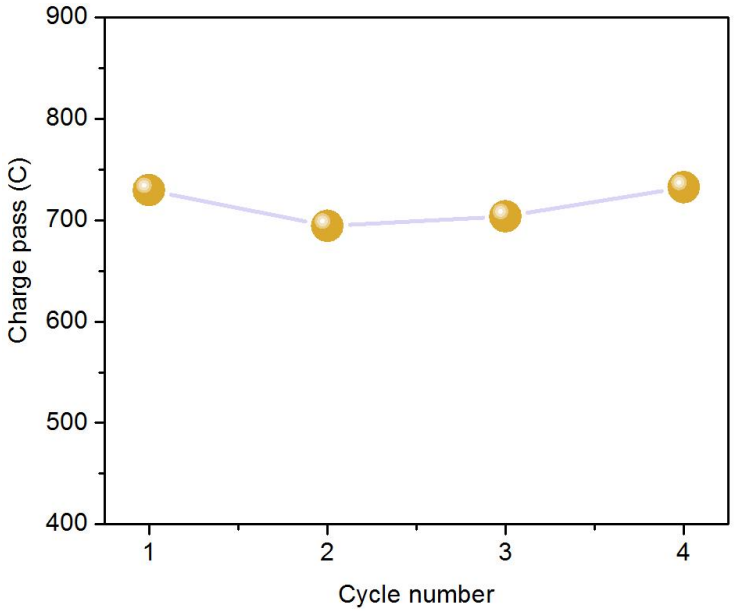

Fig. S31. Charge accumulation in the cycling stability test of the full-cell electrolysis system. Successive chronoamperometry curves are recorded at a high cell voltage of 4.5 V.

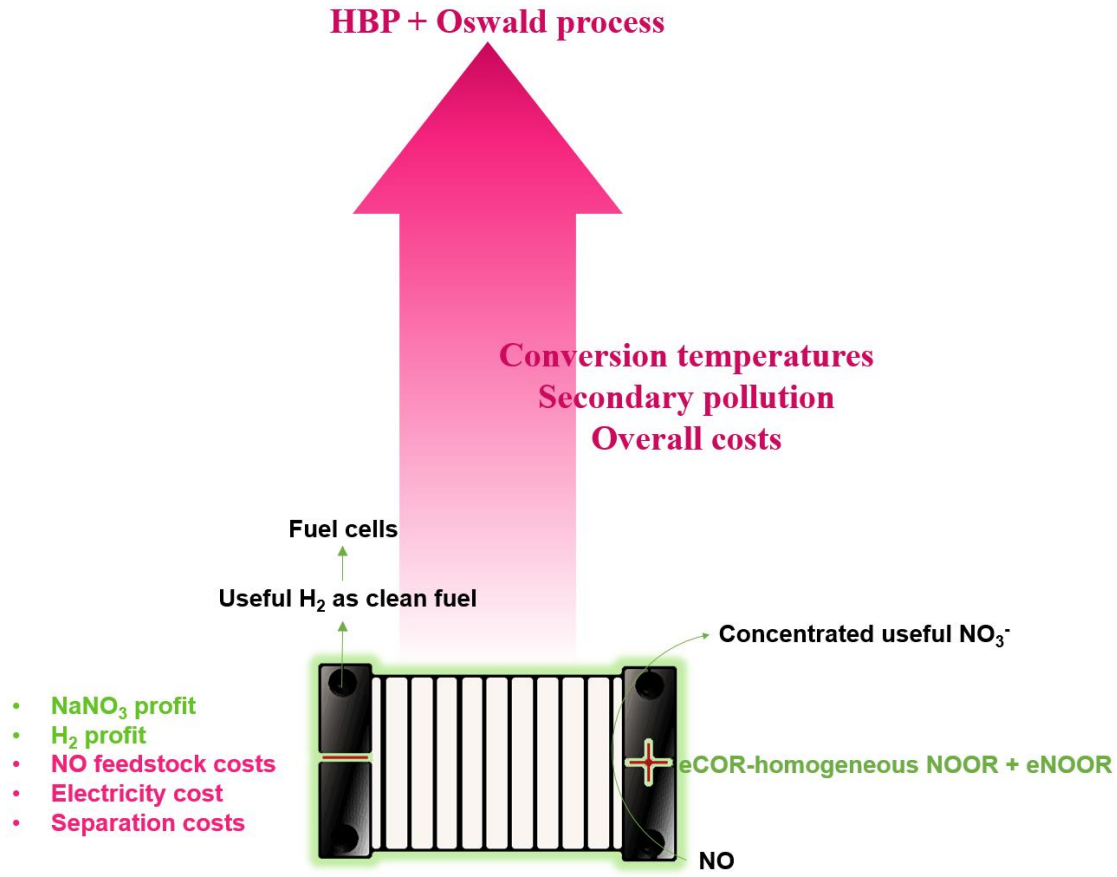

Fig. S32. Sustainable $NaNO_3$ electrosynthesis using NO as feedstock. We present the economic feasibility below.

For preliminary techno-economic analysis (TEA) for the production cost, we assume a 1 cm^2 area of the catalyst is used for the synthesis of $NaNO_3$. The calculation here includes energy, feedstock input, separation costs, H_2 profit, and $NaNO_3$ profit; no other costs associated with practical production or infrastructure were included, which is beyond the scope of this work.

The commercial $NaNO_3$ price is ~ 650 $/MT without transportation cost according to https://www.echemi.com/productsInformation/pid_Rock18871-sodium-nitrate.html. The prices of hydrogen is assumed as 1900 $ t^{-1} based on recently reported work (*Nat. Commun.* 2022, **13**, 5452). Separation costs include the sodium chloride/ sodium nitrate separation. In addition, the electrolyte we used contained a large amount of sodium ions, so NO_3^- productivity was directly used for $NaNO_3$ productivity estimation. The total separation costs are assumed to be 10 % of the electricity cost. Our performance data (Fig. 5) were used to roughly model the electrolyzer system and

calculate the overall energy. We did the calculation below for a particular electrode potential to illustrate the calculation process.

$$P\ (W) = I\ (A) \times V_{cell}\ (V)\ (1)$$

P is the installed power rating in Watts (W), V_{cell} is the cell potential in Volts (V), I is the current passing through the electrode in Amperes (A).

$$FE = nzF/Q\ (2)$$

n refers to molar mass, z refers to Number of transferred electrons

Operation condition: 3.0 V (123.88 mA); Production rate: 0.254 g h^{-1}

$$m_{NaNO3} = 1\ kWh / (3.0\ V * 0.12388\ A) * 0.254\ g\ h^{-1} = \sim 683.5\ g\ (2)$$

Assuming the price of electricity is 0.03 \$/kWh (3 cents/kWh), we can roughly estimate a $NaNO_3$ production cost of ca. \$0.043/kg-$NaNO_3$ without considering the cost of deionized water, NO input and the separation. The price of deionized water is estimated to be 0.008 \$ kg^{-1} based on the recently reported work (*Science* 2021, ***368***, 1228−1233), which adds a small cost to the $NaNO_3$ production cost of 0.043 \$ kg^{-1}. In addition, the price of NO as the reactant in the nitrate production process is assumed zero in that the NO capture cost and NO credit can be equivalent.

It should be noted that the high-purity H_2 gas generated from the anodic chamber can also be collected to reduce the $NaNO_3$ cost. H_2 profit (H_2 FE is assumed as 100 %) can be calculated using the following equations:

$$FE = nzF/Q\ (3)$$

n refers to molar mass, z refers to number of transferred electrons, FF is the Faradic constant (96485 C mol^{-1})

Thus, mass of H_2 produced per hour (at H_2 FE of ~100% according to the GC results)

$$= Q \times FE_{H2} / F / N * n_{H2} = [(100.00 \times 100\ \% / 96485 / 2 \times 2) \times 10^{-6}]\ t = 0.1036 \times 10^{-8}\ t\ (4)$$

Profit of H_2 per hour = mass of H_2 produced per hour ×1900 = 1.97×10^{-6} \$ (5)

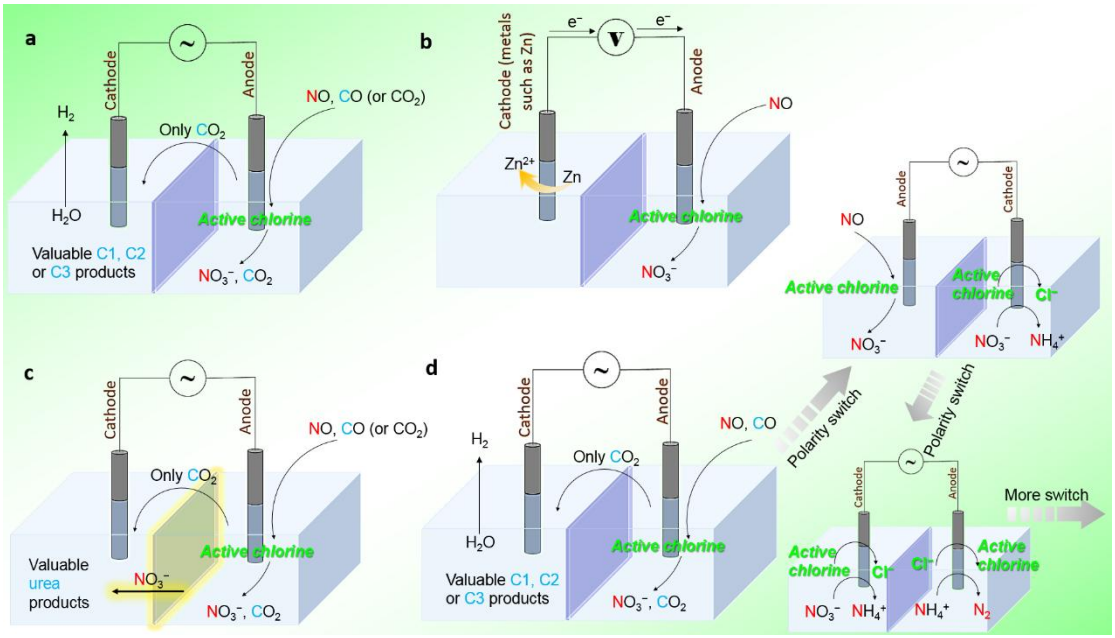

Fig. S33. More ideas for future work. All of the proposed schemes are based on eCOR-mediated NOOR, and have the basic function of NO_3^- electrosynthesis. (a) A mixture of NO and carbon monoxide (NO) passes continuously through the cathodic and anodic chambers to produce not only NO_3^- but also useful carbon-based products, thus achieving more cost-efficient production. In addition, H_2 as gaseous product further increase profits. In the presence of potent oxidant, *i.e.*, the active chlorine, CO_2 would be the only gas left from the anodic chamber, which can be simultaneously electro-reduced to value-added C1 (e.g., formate), C2 (e.g., ethylene) or C3 products (n-propyl alcohol) at the cathode. (b) Schematic illustration of the aqueous metal-NO battery with the capability of achieving harmful NO abatement, nitrate synthesis, and energy output, simultaneously. Compared with eNOOR, the eCOR-mediated NOOOR can great improve the overall conversion efficiency. The catholyte and anolyte can be 1 M KOH and 0.5 M NaCl, respectively, and the bipolar membrane can maintain the different pH of two compartments. During the discharging process, Zn converts to Zn^{2+}, NO converts to NO_3^-, and CO converts to CO_2 (*Acc. Chem. Res.* 2019, **52**, 1721–1729 and *Energy Environ. Sci.* 2021, **14**, 3938–3944). (c) Renewable electricity-powered green synthesis of higher value-added products such as urea based on the eCOR-NOOR. We can replace the proton membrane with a customized anion exchange membrane that only allows NO_3^- to pass through. Subsequently, efficiently

coupling CO_2 reduction with NO_3^- reduction to electrochemically generate urea at the cathode can be achieved. (d) Continuously changing the polarity of the applied potential. To be more specific, after the anodic chamber accumulates enough NO_3^-, the electrode polarity is switched (anode switch to cathode, cathode switch to anode) to electro-reduce the NO_3^- to NH_4^+. Meanwhile, the active chlorine will also be reduced to Cl^-, and then the solution with NH_4^+ can be subjected to air stripping process to obtain high-purity solid NH_4Cl powder and NH_3 solution products. Notably, the electrolyte can continue to be used after the ammonia has been extracted. Moreover, we can also change the anode-cathode polarity again and electro-oxidize the NH_4^+ to N_2.

Table S1. Brief summary of proposed conversion reactions including the eCOR, OER, eNOOR, etc.

Redox reaction	Element (nitrogen-based, chlorine-based, oxygen-based)
$2\mathbf{Cl^-} \rightarrow Cl_2 + 2e^-$, $E^0_{Cl_2/Cl^-}$ = 1.358 V *vs.* SHE (pH=0) = (1.358 + 0.059pH) V *vs.* RHE	Chlorine
$Cl_2 + H_2O \leftrightarrow HClO + \mathbf{Cl^-} + H^+$	Chlorine/Oxygen
$Cl_2 + OH^- \leftrightarrow ClO^- + \mathbf{Cl^-} + H_2O$	Chlorine/Oxygen
$\mathbf{Cl^-} + 2OH^- \rightarrow ClO^- + H_2O + 2e^-$, E^0 = 1.71 V *vs.* RHE	Chlorine/Oxygen
$\mathbf{Cl^-} + H_2O \rightarrow HClO + H^+ + 2e^-$, E^0 = 1.715 V *vs.* NHE (pH=0)	Chlorine/Oxygen
$2\mathbf{H_2O} \rightarrow O_2 + 4H^+ + 4e^-$, $E^0_{O_2/H_2O}$ = 1.229 V *vs.* RHE	Oxygen
$\mathbf{NO} \rightarrow NO^+ + e^-$	Nitrogen/Oxygen
$NO^+ + OH^- \rightarrow HNO_2$	Nitrogen/Oxygen
$HNO_2 + H_2O \rightarrow NO_3^- + 3H^+ + 2e^-$	Nitrogen/Oxygen
$\mathbf{NO} + \mathbf{H_2O} \rightarrow NO_2^- + 2H^+ + e^-$, E^0 = 1.202 V *vs.* NHE	Nitrogen/Oxygen
$\mathbf{NO} + 2\mathbf{H_2O} \rightarrow NO_3^- + 4H^+ + 3e^-$, E^0 = 0.958 V *vs.* NHE	Nitrogen/Oxygen
$2NO_2 + \mathbf{H_2O} \rightarrow HNO_2 + H^+ + NO_3^-$	Nitrogen/Oxygen
$NO_2^- \leftrightarrow NO_2 + e^-$	Nitrogen/Oxygen
$\mathbf{NO} + NO_2 + \mathbf{H_2O} \leftrightarrow 2HNO_2$	Nitrogen/Oxygen
$3HNO_2 \leftrightarrow HNO_3 + NO_2 + 2H_2O$	Nitrogen/Oxygen
$NO_2 \leftrightarrow N_2O_4$	Nitrogen/Oxygen
$N_2O_4 + H_2O \leftrightarrow HNO_2 + HNO_3$	Nitrogen/Oxygen
$NO_2 \leftrightarrow NO_2^+ + e^-$, E^0 = 1.56 V *vs.* NHE	Nitrogen/Oxygen

$\mathbf{NO} + 2ClO^- \rightarrow NO_3^- + 2Cl^-$	Nitrogen/Chlorine
$2\mathbf{NO} + \mathbf{Cl_2} \rightarrow 2NOCl$	Nitrogen/Chlorine
$NOCl + \mathbf{H_2O} \rightarrow 2HNO_2 + HCl$	Nitrogen/Chlorine/Oxygen
$NO_2^- + \mathbf{H_2O} \rightarrow NO_3^- + 2H^+ + 2e^-$, $E^0 = 0.835$ V *vs.* NHE	Nitrogen/Oxygen
$\mathbf{NO} + ClO_2^-/ClO_3^- \rightarrow NO_2 + Cl_2$ $(3NO_2 + H_2O \rightarrow HNO_3 + NO)$	Nitrogen/Chlorine

Note: Anodic chamber of our HER//eCOR-NOOR system involves three main species, *i.e.*, nitrogen species (*e.g.*, NO, NO_2, NO_2^-, NO_3^-), chlorine species (*e.g.*, dissolved Cl_2(aq)), HClO, ClO^-) and oxygen species (O_2, OH^-). Notably, chlorine-containing anions such as ClO_2^-, ClO_3^- or ClO_4^- may also exist in the anolyte, but due to unfavored kinetics for their formation, the main products are considered to be two-electron transfer products (Cl_2, HClO, ClO^-). Considering that various reactions occur in the anodic chamber, we present the possible reactions involved, and all starting reactants/substrates (such as Cl^-) in the table are in bold. Equilibrium potential for the OER is pH-independent of the RHE scale, whereas the reverse is true for eCOR.

Table S2. ICP-OES (PerkinElmer Avio 200) quantification of Co dissolution. Sample A1 is the acidic electrolyte (without dilution) after eCOR electrolysis at 1.4 V_{SCE} for 10 h. Sample A2 is made by dissolving fresh catalyst electrode in strong acids, which is then diluted for characterizations.

Sample	Co $content_{mean\ value}$ (mg L^{-1})
A1	ND
A2	5.508

Note: The limit of detection is 0.007 mg L^{-1}, and no Co can be detected in sample A1. According to the ICP-OES results, the dissolution rate of the Co_3O_4 catalyst during the eCOR-NOOR process is slow, and the loading of the catalyst is determined to be ~9.00 mg cm^{-2}.

Table S3. Performance comparison between our model Co_3O_4 catalyst and previously reported catalyst for Cl^- oxidation.

Electrocatalytic system		E_{RHE}@0.1	Reference
Co_3O_4	0.5 M NaCl, pH=7, 25 °C, scan rate: 2 mV s^{-1}	2.16*	This work
	0.5 M NaCl, pH=2, 25 °C, scan rate: 2 mV s^{-1}	1.82* (1.63)	
	5 M NaCl, pH=7, 25 °C, scan rate: 2 mV s^{-1}	1.91*	
	5 M NaCl, pH=2, 25 °C, scan rate: 2 mV s^{-1}	1.65*	
Pt_1/CNT	1.0 M NaCl, pH=1, 25 °C, scan rate: 10 mV s^{-1}	1.45@0.03	*Nat. Commun.* 2020, **11**, 412
Ti-Ru-Ir based DSA (Siontech Inc., Korea)	1.0 M NaCl, pH=1, 25 °C, scan rate: 10 mV s^{-1}	1.431@0.01	*Nat. Commun.* 2020, **11**, 412
Ti-Ru based DSA ($Ru_{0.3}Ti_{0.7}O_2$, Bayer Materials, Germany)	3.5 M NaCl, pH=3, 80 °C	1.548	*Phys. Chem. Chem. Phys.* 2012, **14**, 7392–7399
Ti-Ru based DSA ($Ru_{0.3}Ti_{0.7}O_2$, Bayer Materials, Germany)	3.5 M NaCl, pH=3, 50 °C, scan rate: 20 mV s^{-1}	1.595	*Chem. Mater.* 2010, **22**, 6215–6217
Ti-Ru-Ir based DSA (Bayer Materials, Germany)	4.0 M NaCl, pH: 3, 25 °C, scan rate: 100 mV s^{-1}	1.872*	*Phys. Chem. Chem. Phys.* 2014, **16**, 13741–13747
$RuTiO_x$	4.0 M NaCl, pH=2, 25 °C, scan rate: 10 mV s^{-1}	~1.77	*Energy Environ. Sci.*, 2019, **12**, 1241–1248
Porous Ir/TiO_2	4.0 M NaCl, pH=3, 40 °C, scan rate = 5 mV s^{-1}, 3500 rpm	~1.80*	*ACS Catal.* 2013, **3**, 1324–1333
RuO_2/Nb:TiO_2-A200	0.6 M NaCl, pH: 6, 25 °C, scan	1.722	*ACS Catal.* 2021, **11**,

E_{RHE}**@0.1A cm^{-2}**: the potential at which the current density reaches 0.1 A cm^{-2}; *****denotes the value of potential without considering iR compensation.

Table S4. Comparison of NO_3^- formation rates for eCOR-NOOR with eN_2OR and eNOOR under ambient conditions.

Reaction	Catalyst	NO_3^- formation rate	Reference
eCOR-NOOR	nanostructured Co_3O_4	790.1 mg cm^{-2} h^{-1} (87715.6 μg h^{-1} $mg_{cat.}^{-1}$)@4.5 V (two-electrode system) 115.45 mg cm^{-2} h^{-1} (12828.17 μg h^{-1} $mg_{cat.}^{-1}$)@2.15 V_{RHE} (three-electrode system)	This work
eN_2OR	AD-Fe NS	6.12 μmol mg^{-1} h^{-1} (379.44 μg h^{-1} $mg_{cat.}^{-1}$, 2.45 μmol cm^{-2} h^{-1})@2.4 V_{RHE}	*ACS Nano* 2022, **16**, 655–663
eN_2OR	Mo–O–C	217.1 ± 13.5 μg h^{-1} $mg_{cat.}^{-1}$@2.35 V_{RHE}	*J. Phys. Chem. C* 2022, **126**, 965–973
eN_2OR	np-$B_{13}C_2$	165.8 μg h^{-1} $mg_{cat.}^{-1}$@2.4 V_{RHE}	*Small* 2021, **17**, 2102814
eN_2OR	OPA-PCN-222(Fe)	110.9 μg h^{-1} $mg_{cat.}^{-1}$@1.6 V_{RHE}	*Appl. Catal. B: Environ.* 2022, **316**, 121673
eN_2OR	Fe-SnO_2	42.9 μg h^{-1} $mg_{cat.}^{-1}$@1.96 V_{RHE}	*Angew. Chem. Int. Ed.* 2020, **59**, 10888
eN_2OR	Ru–Mn_3O_4	35.34 μg h^{-1} $mg_{cat.}^{-1}$@2.0 V_{RHE}	*Adv. Mater.* 2022, **34**, 2108180
eN_2OR	Pd-s PNSs	18.56 μg h^{-1} $mg_{cat.}^{-1}$@1.75 V_{RHE}	*Angew. Chem. Int. Ed.* 2021, **60**, 4474
eN_2OR	Rh/RhO_2	168 μmol h^{-1} $g_{cat.}^{-1}$ (10.42 μg h^{-1} $mg_{cat.}^{-1}$)@1.9 V_{RHE} (0.1 M KOH +0.5 M SO_4^{2-}); 0 μmol h^{-1} $g_{cat.}^{-1}$@1.9 V_{RHE} (0.1 M KOH +0 M SO_4^{2-})	*Angew. Chem. Int. Ed.* 2022, **61**, e202204541
eN_2OR	Ru-doped TiO_2/RuO_2	161.9 μmol h^{-1} $g_{cat.}^{-1}$ (10.04 μg h^{-1} $mg_{cat.}^{-1}$)@2.2 V_{RHE}	*Adv. Mater.* 2020, **32**, 2002189
eN_2OR	$ZnFe_2O_4$	26.4±1.9 μmol h−1 gMO^{-1} (8.06 μg h^{-1} $mg_{cat.}^{-1}$)@1.5 V_{RHE}	*Angew. Chem. Int. Ed.* 2020, **59**, 9418

eN_2OR	$Pd_{0.9}Ru_{0.1}$	77.7 μmol $g_{cat.}^{-1}$ h^{-1} (4.82 μg h^{-1} $mg_{cat.}^{-1}$)@1.7 V_{RHE}	*ACS Catal.* 2021, **11**, 14032–14037
eN_2OR	Pd-MX	45.16 μmol h^{-1} $g_{cat.}^{-1}$ (2.8 μg h^{-1} $mg_{cat.}^{-1}$)@2.03 V_{RHE}	*Chem. Commun.* 2020, **56**, 5779–5782
eN_2OR	Pt foil	0.06 μmol h^{-1} cm^{-2}@2.4 V_{RHE}	*Natl. Sci. Rev.* 2019, **6**, 730–738
eN_2OR	$Au–Nb_2O_{5-x}$	2.29 μg h^{-1} cm^{-2}@2.4 V_{RHE}	*J. Mater. Chem. A* 2021, **9**, 17442–17450
eNOOR	plasma-engraved CC	N/A	*Angew. Chem. Int. Ed.* 2021, **60**, 24605

Note: AD-Fe NS: atomically dispersed active Fe sites on N-doped carbon nanosheets, Mo–O–C: oxygen-coordinated Mo single-atom catalysts, OPA: n-octadecylphosphonic acid, PCN-222(Fe): a porous MOF constructed using $Zr_6O_8(CO_2)_8(H_2O)_8$ hexanuclear clusters as nodes and iron(III) mesotetrakis(4-carboxyphenyl)porphyrin chloride (Fe-TCPP) as linkers, Pd-s PNSs: Pd porous nanosheets, Pd-MX: well-dispersed Pd nanoparticles on MXene nanosheets, CC: Carbon cloth.

Table S5. XPS peaks deconvolution results of Co^{3+} and Co^{2+} under different electrolysis conditions.

	Co^{3+}	Co^{2+}
j_{200} (acidic)	8903767.53825	9121444.369
j_{100} (acidic)	8842741.04675	9064082.364
j_{50} (acidic)	10175178.539	10431078.711
j_{200} (neutral)	10350089.15775	10517088.83275
j_{100} (neutral)	9284946.997	9503798.6115
j_{50} (neutral)	10240256.34675	10560322.8895
Pristine	11163903.945	11523878.443

Table S6. XPS peaks deconvolution results of O1 (lattice O), O2 (absorbed H_2O), and O3 (hydroxyl group) under different electrolysis conditions.

	O1	O2	O3
j_{200} (acidic)	416892.15025	289837.1285	256854.5475
j_{100} (acidic)	389595.71825	248773.184	224117.805
j_{50} (acidic)	455696.31725	304465.8855	305444.685
j_{200} (neutral)	351452.96275	405887.32775	239937.0705
j_{100} (neutral)	444918.43175	314397.864	264092.672
j_{50} (neutral)	452062.484	317247.78875	233679.40925
Pristine	394913.6715	409385.91675	247928.9505

Note: Prior to the XPS characterization, each electrode was thoroughly washed with ultra-pure water to remove attached electrolyte ions (at least 30 s), and the electrode was then dried with high-purity Ar gas and stored in an inert gas for characterization.